AGU PUBLICATIONS

Geochemistry, Geophysics, Geosystems

RESEARCH ARTICLE
10.1002/2016GC006742

Along-strike variations in the Himalayan orogenic wedge structure in Bhutan from ambient seismic noise tomography

Julia Singer[1], Anne Obermann[2], Eduard Kissling[1], Hongjian Fang[3], György Hetényi[1,2,4], and Djordje Grujic[5]

[1]Institute of Geophysics, Swiss Federal Institute of Technology, ETH Zurich, Zurich, Switzerland, [2]Swiss Seismological Service, ETH Zurich, Zurich, Switzerland, [3]Laboratory of Seismology and Physics of Earth's Interior, School of Earth and Space Sciences, University of Science and Technology of China, Hefei, China, [4]Institute of Earth Sciences, University of Lausanne, Lausanne, Switzerland, [5]Department of Earth Sciences, Dalhousie University, Halifax, Nova Scotia, Canada

Abstract The geological units and tectonic structure exposed in the Bhutan Himalaya document significant regional variations, expressed primarily as tectonic windows and klippen. The along-strike variations of these structures and their metamorphic grade are usually associated with the formation of local duplexes in the underlying tectonic units. To investigate these variations and their extent in depth, we image the isotropic shear-wave velocity structure of the orogenic wedge by ambient noise tomography. Group velocities are extracted from cross correlations of ambient seismic noise, recorded by the temporary GANSSER network in Bhutan. The upper crustal structure beneath Bhutan is mapped down to 18 km depth by directly inverting Rayleigh-wave group velocity measurements in the period range between 2 and 20 s with a ray tracing based inversion approach. Our results reveal several distinct high shear-wave velocity anomalies ($\geq$ 3.6 km/s) and reflect the along-strike variations in the upper crustal structure in relation to the alternating tectonic windows and klippen at the surface. In correlation with the surface geology in the northern part of Bhutan, we interpret shallow high shear-wave velocity anomalies as quarzite-dominated rocks or felsic migmatites with large intrusions of leucogranites. High-velocity anomalies in the orogenic wedge in eastern and western Bhutan correlate with the local geometry of the Main Himalayan Thrust and provide evidence for the formation and depth extent of localized duplexes of quartzite dominated lithology in association with the formation of tectonic windows in the Bhutan Himalaya.

Key Points:
- Ambient noise Rayleigh waves reveal first-order upper crustal shear-wave velocity structure in the Bhutan Himalaya orogen
- Along-strike shear-wave velocity variations in the upper crust provide evidence for duplexes at the base of the Himalayan orogenic wedge
- High shear-wave velocity anomaly indicate thrust duplexing of rocks accreted to the Himalayan wedge along the midcrustal ramp of the MHT

Supporting Information:
- Supporting Information S1
- Figure S1
- Figure S2
- Figure S3
- Figure S4
- Table S1

Correspondence to:
J. Singer,
julia.singer@erdw.ethz.ch

Citation:
Singer, J., A. Obermann, E. Kissling, H. Fang, G. Hetényi, and D. Grujic (2017), Along-strike variations in the Himalayan orogenic wedge structure in Bhutan from ambient seismic noise tomography, *Geochem. Geophys. Geosyst.*, *18*, doi:10.1002/2016GC006742.

Received 21 NOV 2016
Accepted 7 FEB 2017
Accepted article online 12 MAR 2017

1. Introduction

Although the Himalayan orogen is traditionally considered to be highly cylindrical, with lithotectonic units and first-order structures that can be followed along its entire strike, investigations over the past years point to significant along-strike variations at the lithospheric scale. The expression of these variations is clearly seen in the surface relief [*Bookhagen and Burbank*, 2010], gravity anomalies [*Berthet et al.*, 2013; *Hammer et al.*, 2013; *Hetényi et al.*, 2016], foreland basin depth [*Burbank et al.*, 1996], and sampled by several seismological experiments [e.g., *Rai et al.*, 2006; *Monsalve et al.*, 2008; *Guo et al.*, 2009; *Huang et al.*, 2009; *Nabelek et al.*, 2009; *Caldwell et al.*, 2013]. Deviations from cylindrical structure are also indicated in the upper crust by tectonic klippen and windows, like the pronounced Tista-Rangit double-window in Sikkim [e.g., *Landry et al.*, 2016] or the crystalline Kathmandu klippe in Central Nepal [*Stöcklin*, 1980].

In the eastern Himalaya, in the region of Bhutan, synformal klippen of the Tethyan sedimentary sequence (TSS) are preserved on top of the Greater Himalaya Sequence (GHS) [e.g., *Kellett et al.*, 2009], whereas antiformal tectonic windows in western and eastern Bhutan expose the Lesser Himalayan Sequence (LHS) beneath the GHS (Figure 1). The exposure of lower-grade, metasedimentary rocks of the LHS in the Paro window and the Kuru Chu half-window in western and eastern Bhutan and the Rangit window in Sikkim (Figure 1) is associated with the formation of underlying duplexes inferred from geological balanced cross sections [*Bhattacharyya and Mitra*, 2009; *Long et al.*, 2011a, 2011b, 2012]. Their lateral extent is assumed to be locally limited to explain the along-strike variations within ~50 km distance in the shallow crustal structure [*Long et al.*, 2011b, 2012] with synformal TSS klippen in central Bhutan (Figure 1).

Conversely along-strike variations in the upper crustal structure and long-term exhumation rates are associated with variations in the geometry of the basal detachment of the Himalayan orogenic wedge, the Main

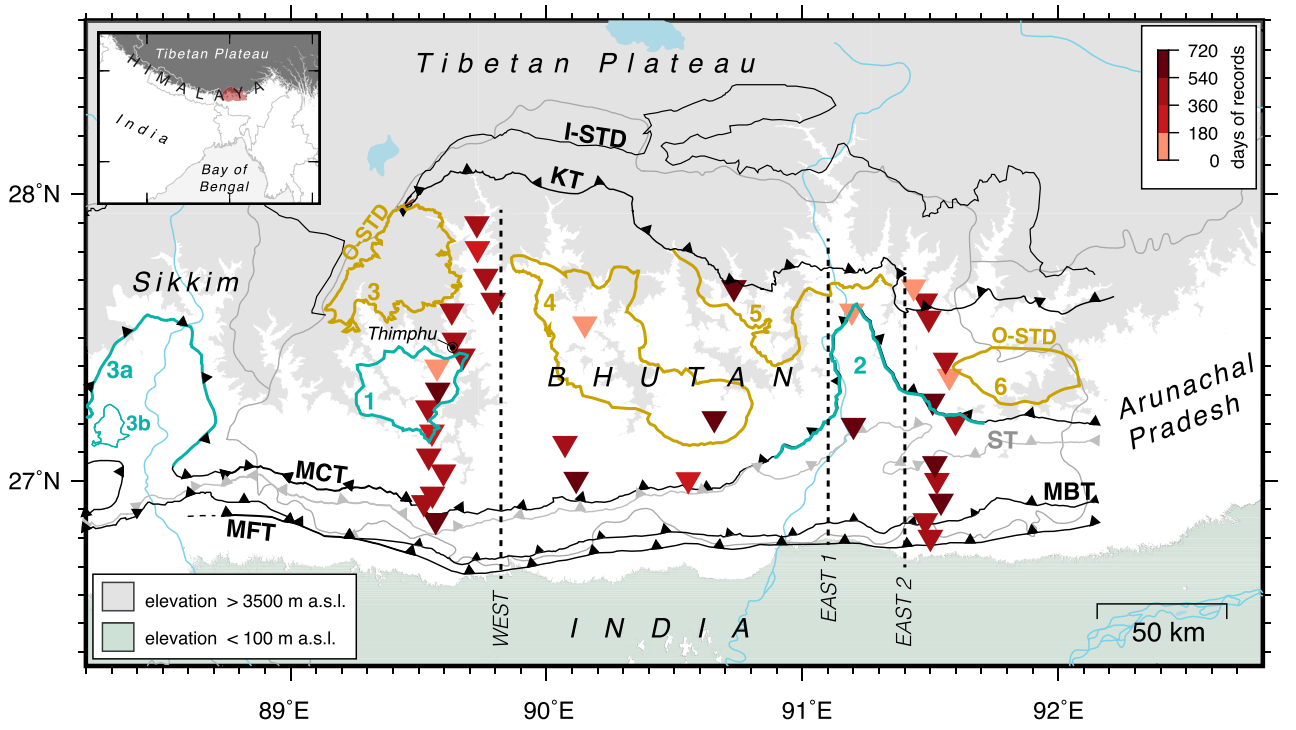

Figure 1. Map of the Bhutan Himalaya with main tectonic structures (modified from *Long et al.* [2011c]). Seismic stations of the temporary GANSSER network are shown by red triangles. MFT, Main Frontal Thrust, MBT, Main Boundary Thrust, MCT, Main Central Thrust, KT, Kakhtang thrust, I-STD, internal South Tibetan detachment, O-STD, outer South Tibetan detachment, ST, Shumar Thrust. Tectonic windows are outlined in turquoise: (1) Paro window, (2) Kuru Chu half-window and (3a) Tista half-window and (3b) Rangit window. Klippen of Tethyan Sedimentary Sequence atop of the Greater Himalayan Sequence is outlined in yellow: (3) Lingshi klippe (4) Dang Chu and Zhemgang klippe, (5) Ura klippe, and (6) Sakteng klippe. The region of the High Himalaya is indicated by the gray area with elevation >3500 m a.s.l.

Himalayan Thrust (MHT), between eastern and western Bhutan based on thermokinematic models [*Coutand et al.*, 2014]. Receiver function studies in these two areas confirm lateral differences in the geometry of the MHT with a midcrustal ramp located in western Bhutan ~80 km north form the MFT trace and a seismogenic, subhorizontal part in eastern Bhutan [*Singer et al.*, 2017], but lack information on structural variations in the overlying orogenic wedge.

To provide geophysical constraints and direct observations in depth of these upper crustal, first-order tectonic structures, we image the isotropic 3-D upper crustal shear-wave velocity structure of the Himalayan orogenic wedge in Bhutan with surface waves from ambient seismic noise. Short-period surface waves ($T < 20$ s) are sensitive to upper crustal variations in shear-wave velocities. These are influenced by various rock properties such as density, temperature, fluids, pronounced foliation, or mineralogy. In the Himalayan orogen, the accreted, folded, or over-thrusted tectonic units differ significantly in their metamorphic grade and mineralogical composition. The southern front is characterized by foreland basin sediments, followed by greenschist facies metasedimentary rocks in the LHS north of the Main Boundary Thrust (MBT) and amphibolite to granulite metamorphic facies rocks of the GHS north of the Main Central Thrust (MCT) with intrusion of leucogranites in the northernmost part of the Higher Himalaya in Bhutan.

First, we measure Rayleigh-wave group velocity dispersions of ambient seismic noise cross correlations from the temporary GANSSER network in Bhutan, to derive 2-D group velocity maps and assess the data quality. Subsequently, we invert for the 3-D shear-wave velocity structure by using a direct inversion scheme. We compare our results to a local 1-D *S* wave velocity model in this region, the local 3-D crustal *P* wave velocity structure defined by a local earthquake traveltime tomography and images of first-order crustal velocity structures defined by receiver functions. Finally, we interpret our results in the context of the surface geology and possible underlying tectonic structures of the Himalayan wedge in Bhutan.

2. Data and Methods

We analyzed continuous records from the temporary seismic GANSSER network (https://doi.org/10.12686/sed/networks/xa) in Bhutan. The network was deployed across the Bhutan Himalaya from January 2013 to November 2014 and consists of two densely spaced south-north arrays in western and eastern Bhutan and eight stations in central Bhutan (Figure 1 and Table S1 in supporting information). The network has a maximum aperture of 220 km and is characterized by heterogeneous interstation distances due to the two denser south-north arrays. We cross correlated the vertical components of the 37 broadband stations (24 Streckeisen STS2 and 13 Nanometrics Trillium Compact) and extracted coherent Rayleigh waves from ambient seismic noise that we then use to derive the 3-D upper crustal shear-wave velocity structure in the region.

2.1. Preprocessing and Computation of Noise Cross correlations

Prior to the cross correlation (CC), a signal preprocessing is applied to the seismic noise records for each station following *Bensen et al*. [2007]. We use the continuous data of the vertical component at each station and down-sample the records to 5 Hz, remove possible major high-frequency spikes and narrow data glitches from them, deconvolve the instrument response and subdivide them into 2 h long segments. On these segments, we apply the following preprocessing: (1) removal of the mean and the long-term trend of the signal, (2) band pass filtering between 0.01 and 2 Hz, (3) running-absolute-mean normalization in the time-domain using temporal weights computed on the waveform filtered in frequency band between 0.02 and 0.67 Hz to reduce the amplitude of precursory signals in the CC caused by earthquakes, and (4) spectrum whitening in the frequency domain.

After the preprocessing, we cross correlate the 2 h long segments between all station pairs and stack them to single time series per station pair. The stacked CCs consist on average of one year of data, with a minimum of 26 days and a maximum of 667 days depending on the operation time of individual stations (Figure 1).

The vertical-vertical component (ZZ) CCs of all station pairs ordered with interstation distance are shown in Figure 2a in the frequency band 0.05–0.1 Hz. We retrieve dominant fundamental Rayleigh surface wave signals in the frequency band 0.05–0.6 Hz. The amplitude of the signals reveals a weak asymmetry between the causal and acausal parts of the CCs over all period ranges. The asymmetry appears more pronounced for west-east oriented stations pairs than for south-north oriented stations pairs (indicated in green and pink, respectively, in Figure 2), likely due to an inhomogeneous distribution of oceanic noise sources as indicated in Figure 2b.

Between 0.1 and 0.4 Hz the vertical CCs are dominated by a zero-lag time signal (Figure 2c). In particular for station pairs with an interstation distance less than 20 km this signal interferes with the vertical component signal of the Rayleigh waves. We tested different preprocessing methods on vertical and horizontal components to remove this interfering signal. Independent of the preprocessing we observe a consistent strong signal on the vertical component and a significantly weaker signal on the horizontal components (Figure S1 in supporting information). This can be interpreted as an indication for a coherent vertical wavefield with a steep incidence angle in the double-frequency microseisms. Previous studies in California and in China [e.g., *Zhang et al*., 2010; *Sheen and Shin*, 2016] attribute such a dominant signal to noise-generated *P* waves. The *P* waves are proposed by to be excited by distant ocean winds during storms in the Pacific [*Zhang et al*., 2010]. As a consequence, we reject CCs of station pairs with distance $<$20 km to measure fundamental Rayleigh-wave group velocities.

2.2. Rayleigh-Wave Group Velocity Measurement

We symmetrize the CC stacks by folding the causal and anticausal part on top of each other to enhance the signal to noise ratio (SNR) and measure the frequency-dependent group velocities between each station pair using the Frequency Time Analysis (FTAN) [*Levshin et al*., 1989]. For the group velocity analysis, we consider only CC stacks, which exceed a SNR of 5 for at least four frequency ranges (between periods of 2 and 24 s with a window length of 8 s and overlap of 6 s) to extract any group velocity information from this station pair. After this automatic quality selection and the removal of CCs with interstation distance $<$20 km (section 2.1), we obtain a CC data set of 395 station pairs from initially 654 computed CC stacks to measure fundamental group velocity dispersion curves.

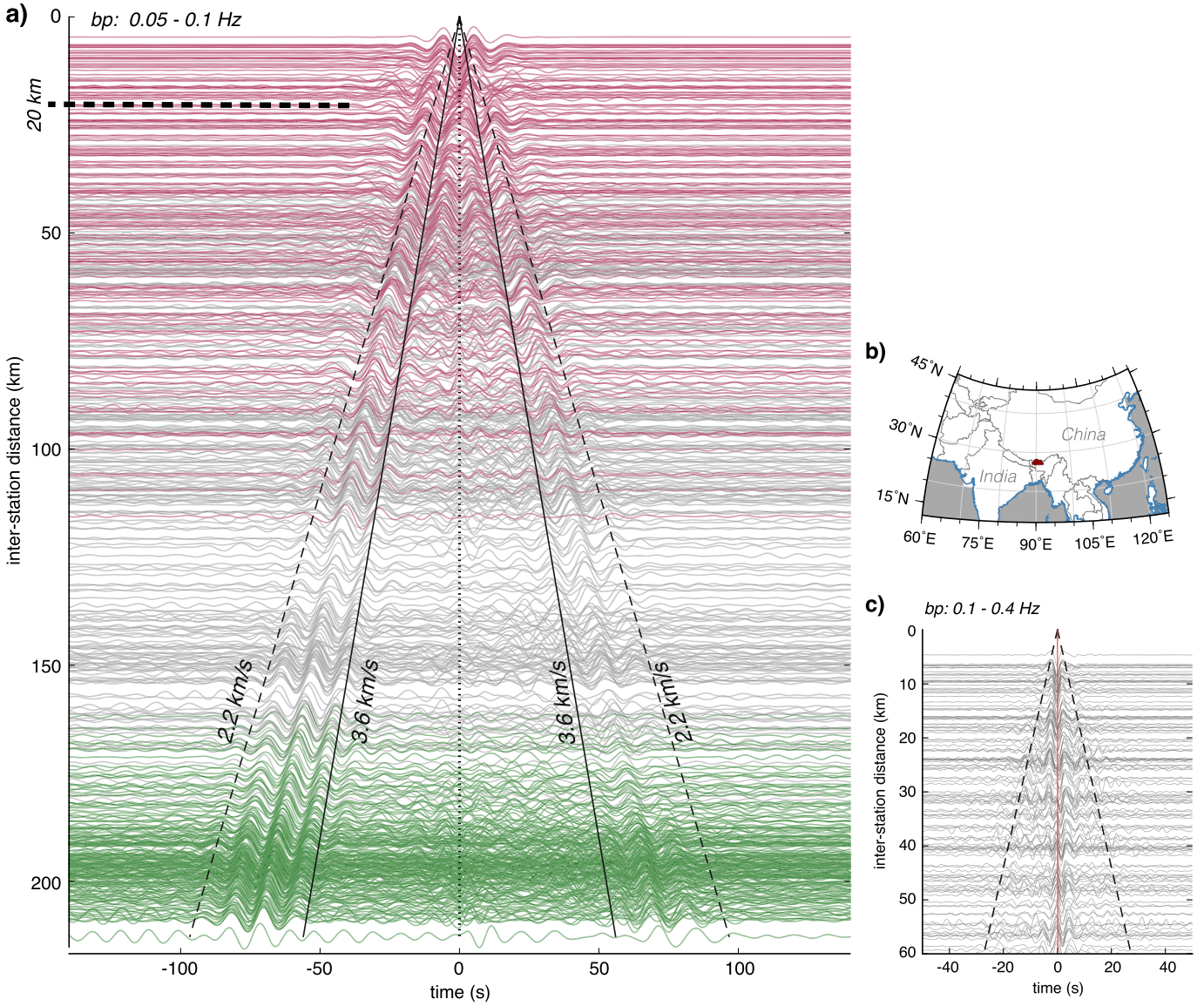

Figure 2. Stacked vertical-vertical component cross correlations (CC), band pass filtered between 0.05 and 0.1 Hz, of all station pairs of the GANSSER network, ordered by interstation distance. Green colored CCs present station pairs oriented in west-east direction and pink colored CCs station pairs with south-north orientation. (b) Map of nearby coastlines to Bhutan. Bhutan is indicated in red, coastlines are shown as blue lines. (c) Dominant zero-lag time signal in CCs for station pairs up to 60 km distance band pass filtered between 0.1 and 0.4 Hz.

The measurement of the dispersion curves with the FTAN is done semiautomatically by using the code of *Mordret et al.* [2013] with a graphical user interface. Each dispersion curve is carefully checked by considering the heterogeneous distance range between station pairs (20–210 km) and the consistency of neighboring station pairs with similar azimuth and distance. In addition to the initial quality selection of CCs for reliable group velocity measurements, we limit the measurements of group velocities to periods with wavelengths of at least one third of the individual interstation distance [*Bensen et al.*, 2007; *Yang et al.*, 2007].

The resulting data set of frequency-dependent group velocity measurements consists of 319 dispersion curves, which comprises periods between 2 and 20 s (Figure 3).

2.3. Inversion for 2-D Group Velocity Maps

Variations in the group velocity measurements at discrete periods are transformed to 2-D group velocity maps using the ray-theoretical tomography approach of *Barmin et al.* [2001] implemented in the ANSWT code of *Mordret et al.* [2013], which includes a Gaussian-shaped lateral smoothing. The computation of 2-D group

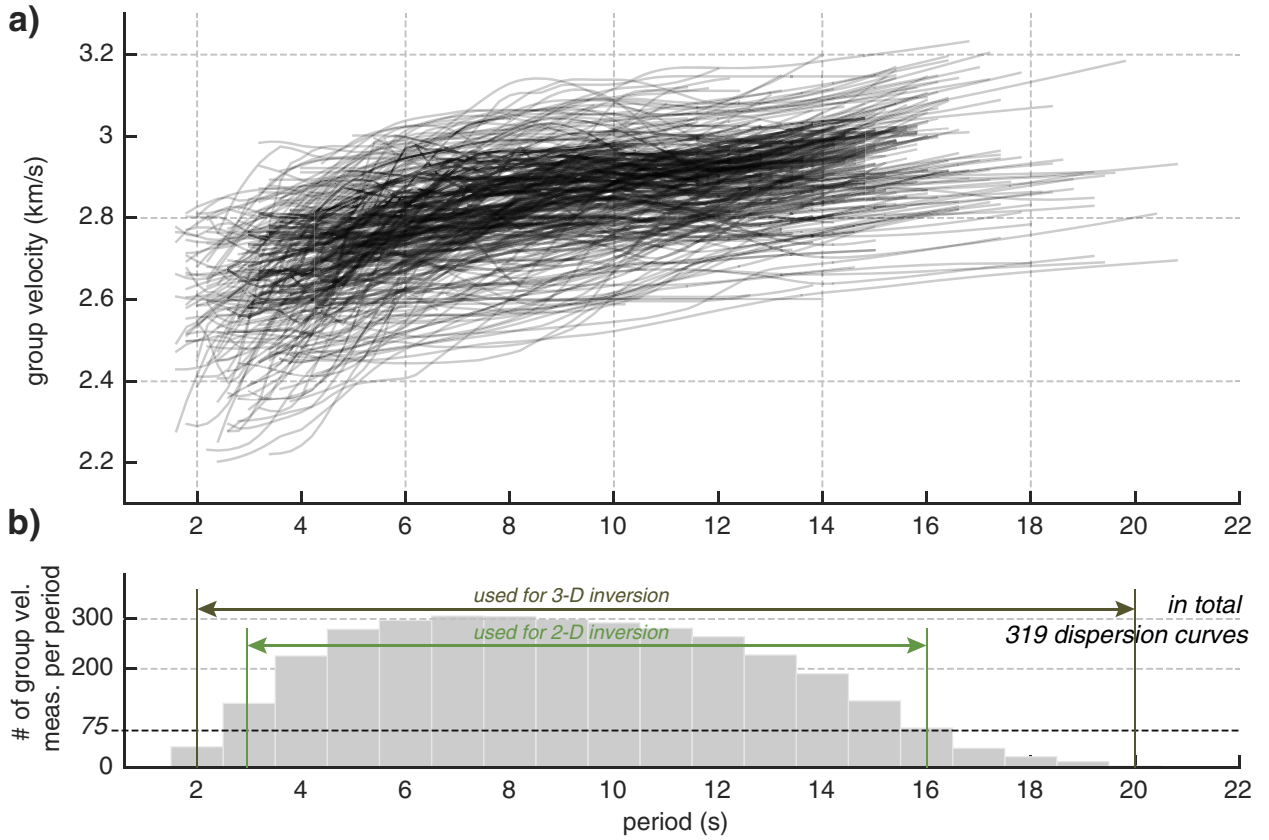

Figure 3. Group velocity dispersion curves of vertical-vertical component, symmetric CCs using the Frequency Time Analysis (FTAN) [*Levshin et al.*, 1989]. CCs for the FTAN are preselected based on signal-to-noise ratio of the precursory signal (details of quality selection are described in section 2.2) to retrieve only high-quality group velocity measurements.

velocity maps at different periods provides a first approximation of the 3-D surface wave velocity structures of the upper crust in Bhutan, besides an estimate on the spatial data coverage. We choose a uniform, relatively large grid size of 20 by 20 km for all periods to better account for the relatively poor azimuthal coverage of measurements in south-north direction compared to well-sampled west-east direction (Figures 4b and 4e). After a trade-off analysis (L-curve analysis) of the regularization inversion parameters, we use a constant correlation length of twice the grid-spacing, a weighting coefficient of the spatial smoothing of 0.2, and 5 as a damping coefficient. For the interpretation of only well-resolved regions of the derived 2-D velocity maps, we compute the resolution matrix as described by *Barmin et al.* [2001] and extract the resolution diagonal element (RDE) for each cell. The leakage to off-diagonal elements in the resolution matrix is weak and indicates a low influence of measurements of neighboring cells on group velocities obtained in individual cells. In combination with the lateral ray density and azimuth coverage (Figures 4b and 4e), fairly well to well-resolved areas are defined within the RDE contour line of 0.14 (Figures 4c and 4f).

The results of the 2-D velocity inversion reveal a general south-north increase of shear-wave velocities across the Himalayan orogenic wedge for all periods (Figures 4a and 4d), which correlates well with variations in the dispersion measurements projected along straight rays between station pairs (Figures 4b and 4e). Along-strike variations between western and eastern Bhutan are indicated at different periods, as shown in Figures 4b and 4e for 6 s and 14 s, respectively. Relatively low velocities (−4%) are derived for central Bhutan and a high-velocity anomaly (+6%) in western Bhutan at the northeastern side of the Paro window. As a consequence of the predominant azimuthal ray coverage in east-west direction, a lower resolution of along-strike variations is expected, causing lateral smearing.

2.4. Inversion for 3-D Shear-Wave Velocity Structure

We use the method, presented in *Fang et al.* [2015] to directly invert group velocity measurements to a 3-D shear velocity model of the upper crust. The method is similar to the approach of *Boschi and Ekström* [2002]

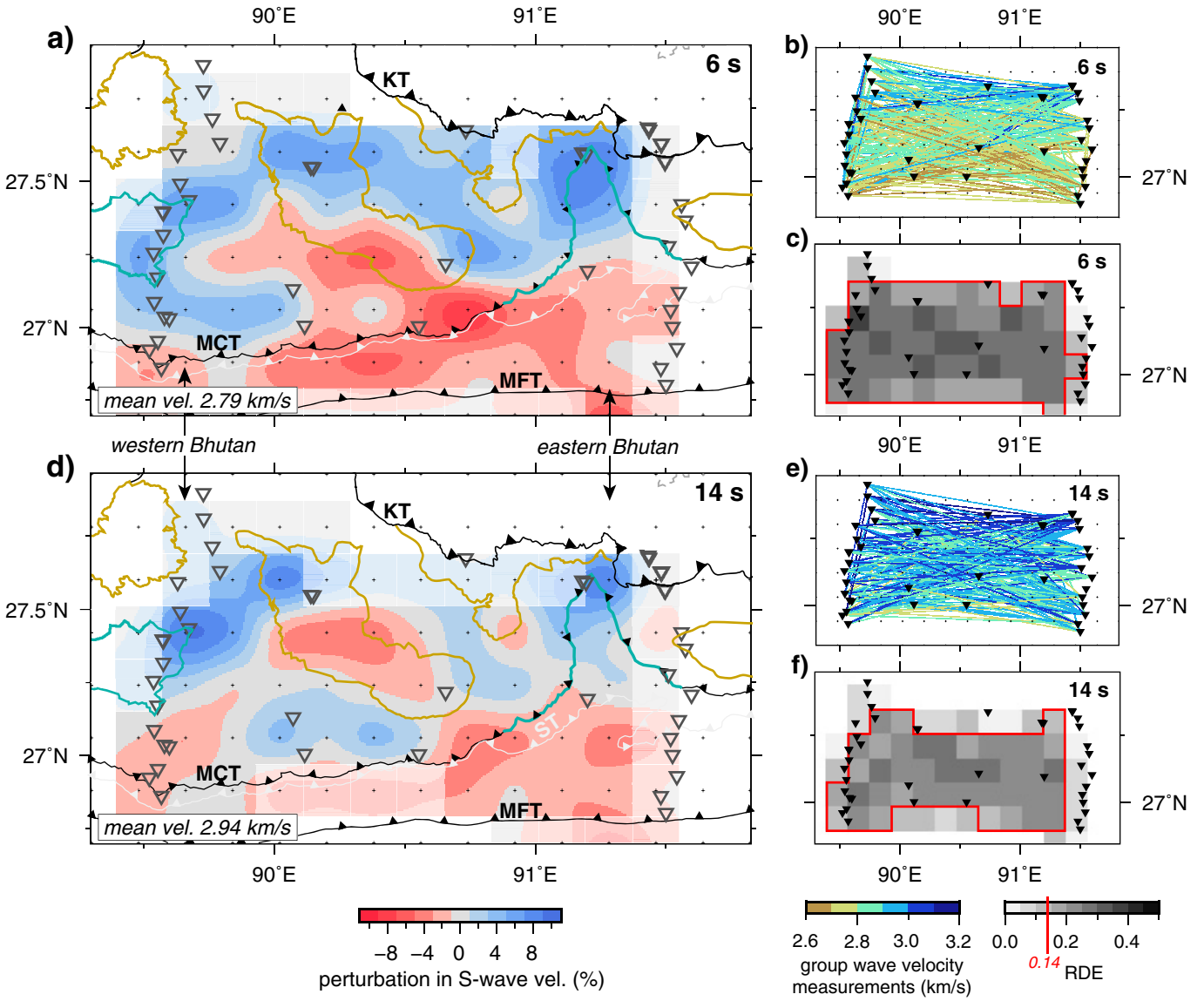

Figure 4. Rayleigh-wave group velocity maps at (a) 6 s and (d) 14 s. The ray coverage for both maps, based on simple straight ray paths between station pairs, are shown in Figures 4b and 4e, respectively. The colors of the rays in Figures 4b and 4e reflect the corresponding group velocity measurement of each station pair. In Figures 4c and 4f, the formal resolution of the 2-D inversion is represented for both periods by the resolution diagonal element (RDE) defined by the resolution matrix. Areas outside fairly well to well-resolved areas in the group velocity maps in Figures 4a and 4d are masked with a minimum RDE value of 0.14, represented by a red line in the resolution in Figures 4c and 4f (see section 2.5). The significance level of velocity variations is approximately ±1%.

and *An et al*. [2009] but with frequency-dependent ray tracing. The 3-D inversion takes into account deviations in great circle wave paths of surface waves, which turns out to be relevant for complex velocity structures [*Young et al*., 2011; *Lin et al*., 2013], common for the upper continental crust. An intermediate step of inverting for group or phase velocity maps is not required. Surface wave dispersion measurements are inverted in a nonlinear scheme directly to a 3-D shear-wave velocity model with the help of a combined sensitivity matrix, which incorporates depth sensitivity kernels. Ray paths of the surface waves are iteratively updated using the fast marching method of *Rawlinson and Sambridge* [2004] with the newly inverted velocity model and incorporated in an updated sensitivity matrix. The sensitivity of the surface waves to density and compressional velocities is considered by using an empirical relationship based on *Brocher* [2005]. To account for effects of noise and nonuniformity in the data coverage, as indicated by the 2-D velocity maps (Figure 4), we use a smoothing of the model term in the inversion as regularization. We parametrize the region in a lateral grid of 10 by 10 km and define depth grid nodes at 0, 2, 4, 6, 8, 11, 14, 18, and 22 km. The

nonuniform depth parameterization with increasing grid-spacing follows the decreasing depth resolution of surface waves. The lateral grid-spacing is chosen to be only half the cell width of the group velocity maps to adopt to a reasonable ratio of the vertical-to-lateral grid parameterization for the 3-D inversion [*Kissling et al*., 2001]. In the inversion, we neglect the short wavelength topographic effects of the high Himalayan relief and topographic effects of the network. In relation to the depth resolution of our data set with periods of 2–20 s, station elevation differences of up to 2.5 km of our network are not sufficient to cause major distortions in the obtained velocity model.

2.5. Resolution Tests

To determine the resolution of the inversion results, synthetic tests of characteristic model structures [*Husen et al*., 2009] are used in combination with the derivative weighting sum (DWS). The DWS represents the total ray length in the cell. With the DWS and synthetic test results we define fairly well resolved regions in the model, similar to the resolution diagonal element (RDE) of the resolution matrix [*Kissling et al*., 2001; *Gritto et al*., 2013] used for the group velocity maps in Figure 4.

Based on different characteristic synthetic velocity models, we solve the forward problem for the given station pairs of our data set. The synthetic input model of Figure 5 has velocity anomalies of $\pm$10%, or $+$7.5% of variable size and geometry that represent realistic velocity structures in our study area (input anomalies are highlighted by dashed red and blue lines). The background velocity is defined by a simple 1-D velocity model with a constant depth gradient, roughly following the group velocity measurements for 3 s with 2.6 km/s for the uppermost layer, and the average upper crustal *S* wave velocity from the minimum 1-D velocity model in Bhutan [*Singer et al*., 2017] of 3.6 km/s for 20 km depth. The so-called "minimum" 1-D velocity model for Bhutan was derived by solving the coupled hypocenter-velocity problem with the program VELEST [*Kissling*, 1988] for well-locatable local earthquakes recorded by the GANSSER network [*Singer et al*., 2017]. This type of 1-D velocity model yields a global minimum data fit and represents the average 1-D velocity structure of a region.

We add 2% of random noise to the synthetic data before inverting the data set with the same regularization and grid parameterization as for the inversion of the real data. For the smoothing we use a weighting of 2, after testing different parameters with simple synthetic models and a sparsity fraction parameter for the sensitivity matrix of 0.15.

The synthetic tests reproduce the predefined large-scale velocity pattern of the input model (Figure 5). As expected, the resolution is dominated by the ray coverage in west-east direction (Figures 4b and 4e). Lateral velocity variations are resolved more accurately in south-north direction within 10 km, as already indicated in the group velocity maps (Figure 4). The low-velocity anomaly in the center of Bhutan (Figures 5a and 5b) is well recovered with respect to its south-north extent, but encounters significant smearing effects in the west-east direction. Velocity anomalies of amplitudes in the order of $\pm$10% perturbation are retrieved well in areas of dense data coverage and in the center of velocity anomalies at depths between 6 and 14 km (Figures 5a–5e). In Figure 5 and the following figures, we only show inversion results for areas, which are sufficiently well-constrained by the data coverage as defined by the DWS (as shown, e.g., in Figures 4b and 4e for group velocity maps at 6 and 14 s).

In comparison to the horizontal resolution, the vertical resolution is less well-constrained by the 3-D inversion as expected from the inherent lower sensitivity of surface waves to velocity variations with depth, in particular to first-order discontinuities. Consequently, we use a higher DWS threshold for well-constrained areas at greater depths to account for the longer wavelengths of surface waves with depth. Vertical velocity variations are imaged as smooth velocity gradients and require a minimum thickness of 4–6 km to be resolved at shallow depth (e.g., low-velocity anomaly in southeastern Bhutan in Figure 5d). From the synthetic tests, we infer a maximum depth of well-resolved velocity variations with reliable information at 14 km. This lower bound of the depth resolution is consistent with the maximum depth sensitivity of our longest group velocity data, of approximately 16 s (Figure 6a).

3. Tomographic Results and Interpretation

3.1. 3-D Shear-Wave Velocity Structure

The results of the 3-D inversion confirm the general characteristics of the 2-D group velocity maps (Figure S3 in supporting information), but provide more detailed information on the depth structure and locations

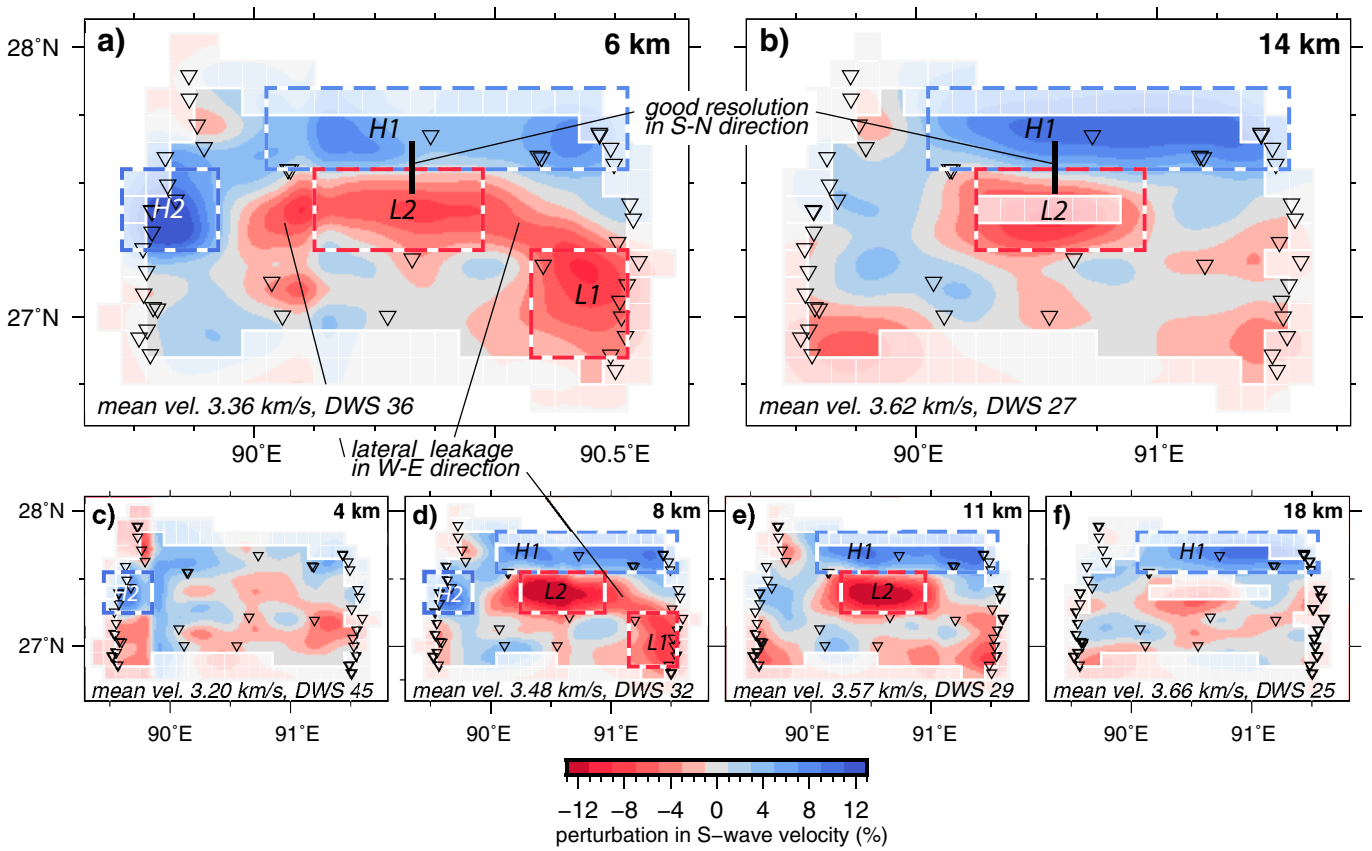

Figure 5. Synthetic test of the 3-D surface wave inversion with characteristic crustal velocity anomalies of the orogenic wedge in Bhutan. Velocity anomalies of the input model at different depths are outlined by boxes, the color of these boxes indicate the amplitude of the anomaly, with deviations of 7.5% and 10% to the background velocity model. Poorly resolved areas at each inversion depth layer are diminished in intensity by using the derivative weight sum (DWS) (see section 2.5).

of first-order velocity anomalies. The exact location of specific velocity anomalies, either imaged as group velocity anomalies in the 2-D maps or isotropic shear-wave velocity anomalies in the 3-D structure, can vary due to differences in parameterizations and approximations used in these two different inversion methods (see Text S1 and Figures S2 and S3 in the supporting information for more details). We derive overall well-constrained shear-wave velocities between 3.0 and 3.8 km/s in the depth range between 4 and 14 km. Velocities down to 18 km depth are less well-constrained and are only partly resolved in the study region (Figure 6). Velocity depth profiles from different locations in the study region indicate clear lateral variations in the shear-wave velocity structure of the orogenic wedge between its southern part (profile B in Figure 6a) in the region of the LHS and the GHS in the northern part (profile A in Figure 6a).

Based on the resolution tests, we can define four dominant velocity anomalies in the orogenic wedge in Bhutan within the extent of the GANSSER network: (1) a high-velocity anomaly north of central and eastern Bhutan close to the Kakhtang thrust (KT) with velocities ~3.8 km/s (hiN in Figures 7b and 7c), (2) a high-velocity area in western Bhutan slightly north of the Paro window (hiW in Figures 6 and 7) with similar high shear-wave velocities like the northern anomaly, (3) a shallow high-velocity area with a maximum depth extent of 12 km between the MBT and MCT in eastern Bhutan (hiE in Figures 6 and 7) and in between, (4) a low-velocity region in the upper crust of around 100 km length in central Bhutan (loC in Figure 6).

To interpret these main velocity anomalies in relation to the tectonic structure of the Bhutan Himalaya, we compare our results with the minimum 1-D shear-wave velocity model using *S* phase body waves of local earthquakes [*Singer et al.*, 2017] (see section 2.5) and the MHT geometry in eastern and western Bhutan defined by receiver functions and earthquake clusters by *Singer et al.* [2017].

Shear-wave velocities derived by the minimum 1-D velocity model [*Singer et al.*, 2017] of around 3.6 km/s for the upper crust agree with velocities of our 3-D model below 8 km depth in northern part of Bhutan, for

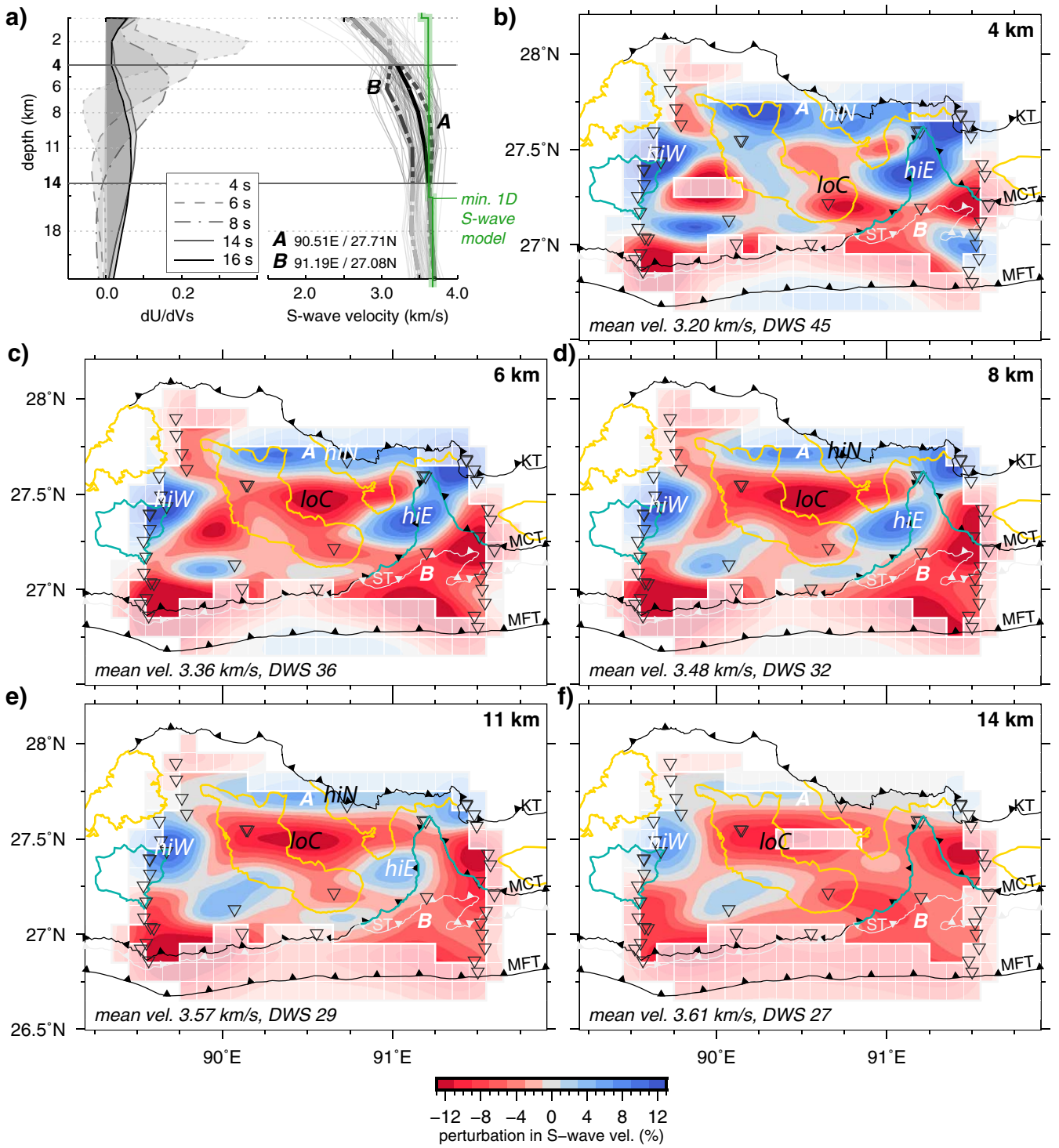

Figure 6. Shear-wave velocity structure of the orogenic wedge in Bhutan derived by the 3-D surface wave inversion. (a) 1-D depth sensitivity kernels of Rayleigh-wave group velocities (dU/dVs) at different periods [*Herrmann*, 2013] (left) and inversion results of shear-wave velocity structure for individual cells (right). The initial 1-D velocity model for the inversion is indicated by the bold black profile. Velocity profiles indicated in Figure 5a with A and B represents the shear-wave velocity structure in the location A and B on the horizontal sections in Figures 6b–6f and green line indicates the upper crustal *S* wave velocity defined by the minimum 1-D *S* wave velocity model [*Singer et al.*, 2016]. (b–f) Horizontal cross sections of the obtained 3-D shear-wave velocity models. Lateral velocities perturbations are shown relative to the velocity defined by the input model. The significance level of velocity variations is approximately ±1%. Well-resolved areas are defined by the DWS similar to Figure 5. Seismic stations of the GANSSER network are shown as black triangles. HiW—high-velocity anomaly in western Bhutan; HiE—high-velocity anomaly in eastern Bhutan; HiN—high-velocity anomaly in northern Bhutan; loC—low-velocity anomaly in central Bhutan. Tectonic surface structures (main thrusts, windows, and klippen) of the Bhutan Himalaya are projected on each depth section for reference as shown in Figure 1.

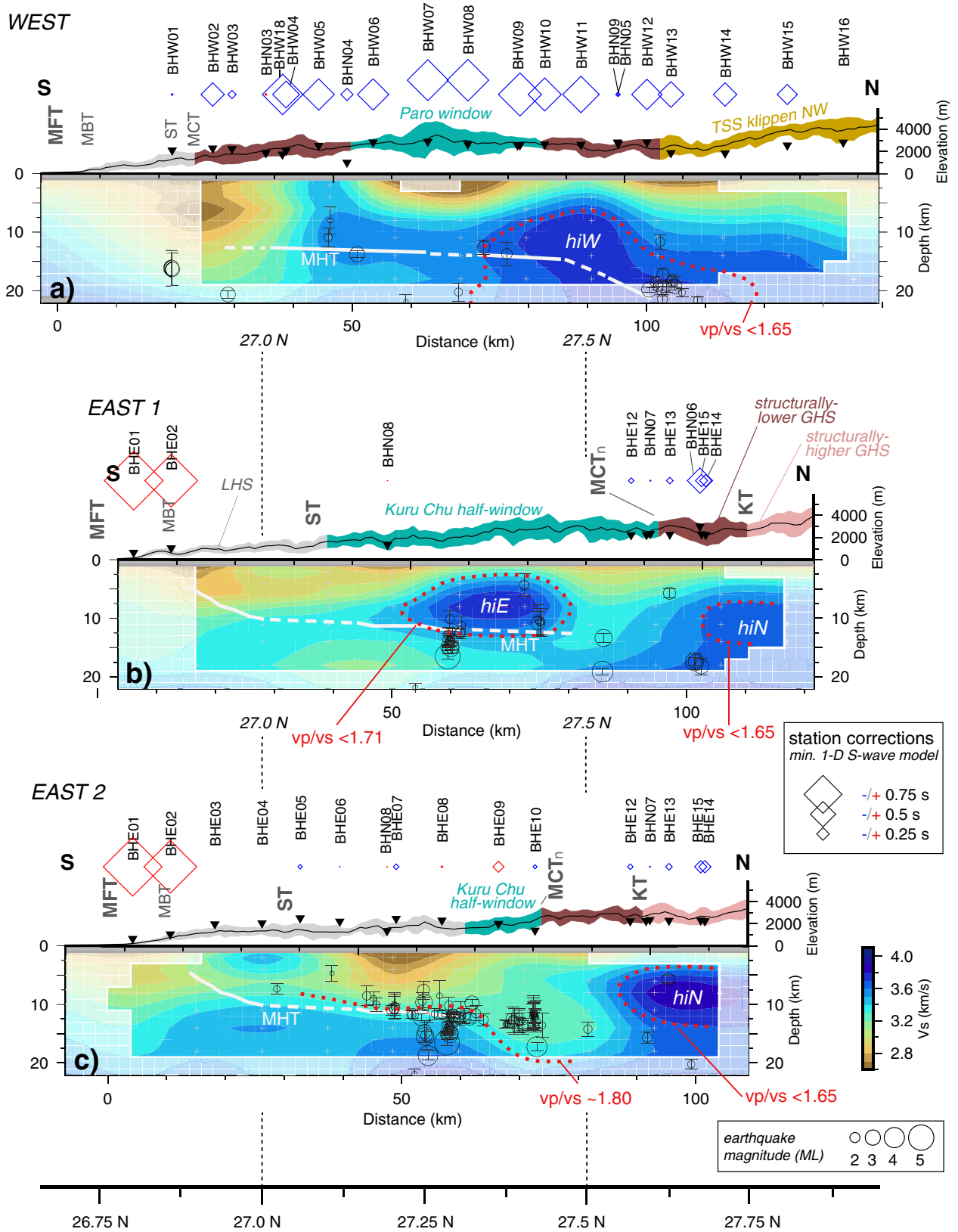
WEST
BHW01
BHW02
BHW03
BHN03
BHW18
BHW04
BHW05
BHN04
BHW06
BHW07
BHW08
BHW09
BHW10
BHW11
BHN09
BHN05
BHW12
BHW13
BHW14
BHW15
BHW16
S
N
MFT
MBT
ST
MCT
Paro window
TSS klippen NW
4000
2000
0
Elevation (m)
MHT
hiW
a)
vp/vs <1.65
Depth (km)
Distance (km)
27.0 N
27.5 N
EAST 1
BHE01
BHE02
BHN08
LHS
MCTn
BHE12
BHN07
BHE13
BHN06
BHE15
BHE14
structurally-lower GHS
structurally-higher GHS
KT
Kuru Chu half-window
hiE
hiN
b)
vp/vs <1.71
vp/vs <1.65
station corrections
min. 1-D S-wave model
-/+ 0.75 s
-/+ 0.5 s
-/+ 0.25 s
EAST 2
BHE03
BHE04
BHE05
BHE06
BHN08
BHE07
BHE08
BHE09
BHE10
c)
vp/vs ~1.80
vp/vs <1.65
Vs (km/s)
4.0
3.6
3.2
2.8
earthquake magnitude (ML)
2 3 4 5
26.75 N
27.0 N
27.25 N
27.5 N
27.75 N

Figure 7.

example, for position A in Figure 6. The discrepancy at shallower depth (<8 km) of these different shear-wave velocity models can be explained by the higher sensitivity of surface waves to resolve local velocity variations close to the surface compared to the significantly lower sensitivity of local earthquake body waves to near-surface velocity variations.

Besides the velocity structure, the minimum 1-D velocity model provides first-order estimates on deviations in the shallow velocity structure beneath each station, defined as station corrections (expressed in seconds) in relation to a reference station. Station corrections with a negative value indicate earlier phase arrival times of earthquake signal, i.e. higher velocities beneath the station and vice versa. The shear-wave velocity anomalies indicated by station corrections (Figure S4 in supporting information), with a predominant negative correction in western Bhutan and less pronounced negative or even positive corrections in eastern Bhutan agree well with the first-order lateral shear-wave velocity anomalies derived by ambient noise tomography (Figures 7 and 8).

The comparison of the 3-D upper crustal shear-wave velocity structure with the MHT in eastern and western Bhutan, which is partly imaged by receiver functions in these regions, shows a clear correlation between the lower bound of the high-velocity anomaly in eastern Bhutan (hiE) and the segment of the MHT at ~12 km depth (white line in Figures 7b and 8a). In western Bhutan, the distinct high-velocity anomaly between 4 and 18 km depth (hiW) is located on top of the southern edge of the midcrustal ramp, extending subhorizontally toward the south (Figures 7a and 8a), consistent with the subhorizontal segment of the MHT at 14 km in this area [*Coutand et al*., 2014; *Roux-Mallouf et al*., 2015; *Singer et al*., 2017]. A sharp contrast in the 3-D shear-wave velocity model in association with the MHT, however, is not resolved due to the intrinsic low sensitivity of surface waves to first-order seismic discontinuities at depth. Furthermore, the maximum depth sensitivity of our period range is around 18 km, only slightly beneath the MHT [*Coutand et al*., 2014; *Singer et al*., 2017] and makes it difficult to resolve this tectonic interface.

3.2. Tectonic Implications for the Himalayan Orogenic Wedge Structure

The structurally higher GHS, in the hanging wall of the Kakhtang thrust (KT) is dominated by migmatitic orthogneisses and paragneisses with numerous intrusions of Miocene leucogranites [*Kellett et al*., 2009, 2010; *Grujic et al*., 2011]. In contrast, rocks of the structurally lower GHS, in the footwall of the KT are assigned to amphibolite metamorphic facies [*Warren et al*., 2011] and comprise fewer and smaller leucogranite intrusions. In central Bhutan, the hiN is in the footwall of the KT while in eastern Bhutan it may be in its hanging wall (Figure 8a). We suggest that this high shear-wave velocity zone might reflect larger volumes of felsic migmatites and leucogranite with a high fraction of quartz-feldspar in the upper crust, as it is indicated by the surface geology in northern Bhutan [*Long et al*., 2011c]. Laboratory experiments for quartzite and quartz-dominated metamorphic rocks reveal such high velocities for shear-waves, but also a less pronounced *P* wave velocity increase [*Christensen*, 1996], leading to a low vp/vs-ratio for such rocks. In a first-order approximation, we estimate the vp/vs-ratio based on our 3-D surface wave results and a local earthquake *P* wave velocity tomography of the crust by *Diehl et al*. [2015] to provide additional constraints on the seismic characteristics of the imaged shear-wave velocity anomalies. However, due to strong differences in the sensitivity of the two tomographic methods and model parameterization of the two inversion applications, the calculated vp/vs-ratio must be considered as a rough approximation and we extract only a general vp/vs-ratio instead of small-scale local variations.

For the northern high-velocity anomaly, extending from central to eastern Bhutan at the front of the High Himalaya (hiN in Figures 6 and 7) this rough approximation indicates a low vp/vs-ratio of 1.65 in good

Figure 7. Shear-wave velocity variations across the orogenic wedge and in relation to the tectonic surface structure, seismicity [*Diehl et al*., 2015] and *P* wave velocities [*Diehl et al*., 2015]. Locations of vertical cross sections are indicated in Figure 1. Abbreviations of shear-wave velocity anomalies (hiW, hiE, and hiN) are the same as defined in Figure 6. Fine, gray crosses indicate grid nodes of 3-D inversion. Rectangles on top of each profile represents station corrections of minimum 1-D velocity model [*Singer et al*., 2016] for each station (black triangle). The reference station of the minimum 1-D model is located in Central Bhutan on the Dang Chu and Zhemgang klippe. MHT geometry defined by receiver functions in eastern and western Bhutan [*Singer et al*., 2016] are presented by solid gray lines, dashed gray lines indicate interpolation. Earthquakes with well-constrained hypocenters (≥ 10 observations and maximum azimuthal gap without observation of ≤ 200°) recorded during the 2 year recording period of the GANSSER network [*Diehl et al*., 2015] within ±20 km distance are projected on each vertical cross section as black circles with focal depth uncertainties. Mean topographic profile within ±20 km distance to profile line is represented by the bold black line and standard deviation by the shaded gray area. LHS—Lesser Himalayan Sequence and GHS—Greater Himalayan Sequence.

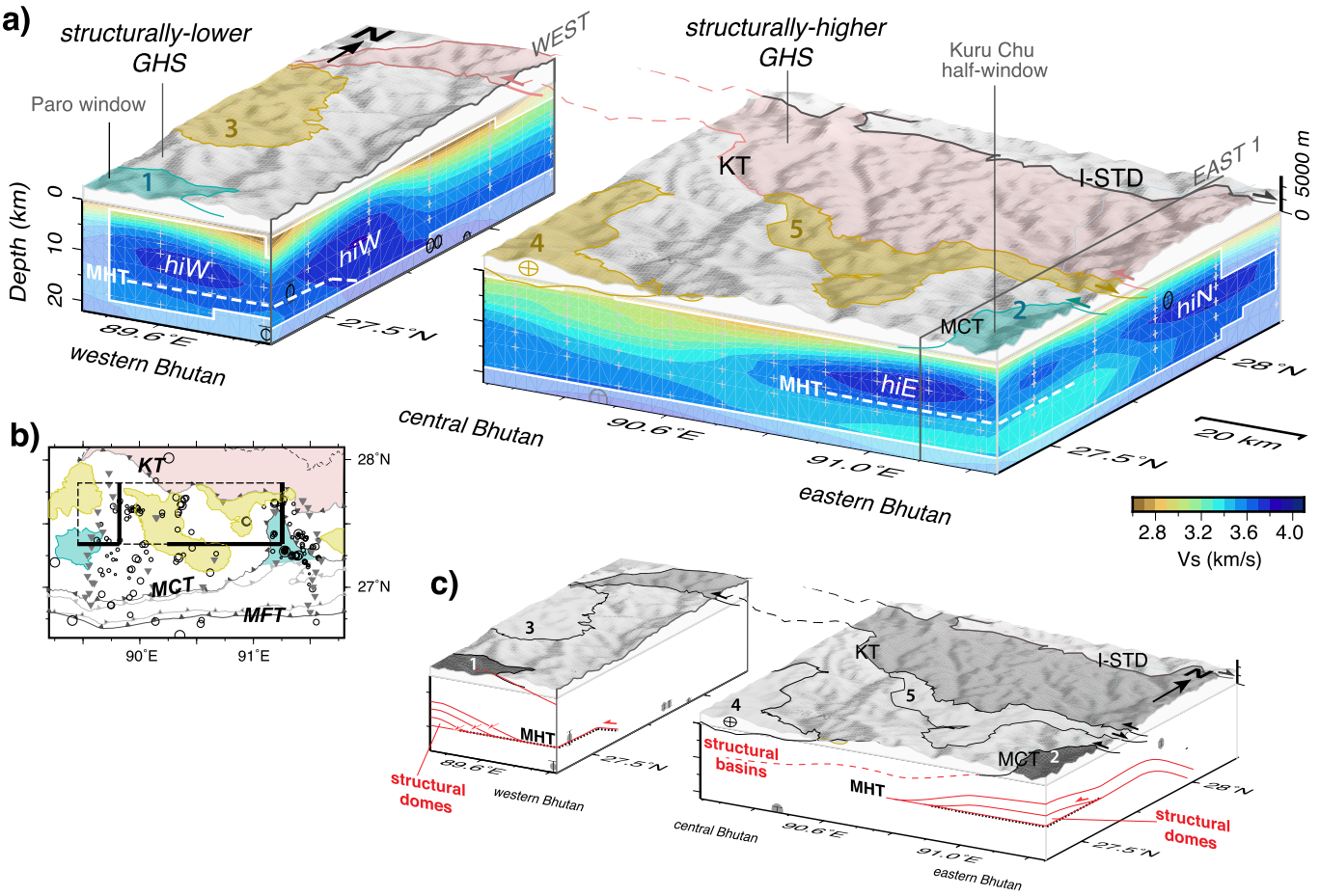

Figure 8. (a) Along-strike variations of upper crustal shear-wave velocity structure between western and eastern Bhutan in relation to the surface geology (see caption of Figure 1 for more details). Fine, gray crosses indicate grid nodes of 3-D inversion. Abbreviations of shear-wave velocity anomalies (hiW, hiE, and hiN) are the same as defined in Figure 6. Earthquakes with well-constrained hypocenters ($\geq$ 10 observations and maximum azimuthal gap without observation of $\leq 200^{\circ}$) recorded during the 2 year recording period of the GANSSER network [*Diehl et al*., 2015] within $\pm$5 km distance are projected on each vertical side of the block as black circles with focal depth uncertainties. (b) Tectonic map of Bhutan with TSS klippen (yellow) and windows (turquoise). Dashed box indicates location of blocks shown in Figure 8a. Black circles indicate earthquake locations of well-constrained hypocenters (same criteria and earthquake catalog like for a)). Stations of the GANSSER network are presented as gray triangles. (c) Simplified sketch of underlying localized duplexes at the base of Himalayan orogenic wedge in the region of tectonic windows in eastern and western Bhutan based on results shown in Figure 8a.

correlation with the mentioned laboratory experiments for quartzite and quartz-dominated metamorphic rocks [*Christensen*, 1996] and high fraction of quartz-feldspar in the felsic migmatites and leucogranite in this area. Such a low vp/vs-ratio has also been reported for the upper and middle crust beneath the High Himalaya in eastern Nepal and beneath southern Tibet by *Monsalve et al*. [2008] in correlation with high *P* and *S* wave seismic attenuation [*Sheehan et al*., 2014].

In western Bhutan where an equivalent upper crustal high-velocity anomaly is absent near ~27.6°N (Figure 7a), the KT strikes in the NW direction and the structurally lower GHS with few leucogranite intrusion extends further to the north by around ~30 km (Figure 1). We interpret this difference in the near-surface geology as additional evidence for the correlation of high upper crustal shear-wave velocities with felsic GHS rocks. Moreover, the TSS klippe atop the GHS in northwestern Bhutan, the Lingshi klippe [e.g., *Kellett and Grujic*, 2012] (labeled as 3 in Figures 1 and 8a, 8b) presumes a local change in the underlying tectonic structure of the orogenic wedge, in comparison to central and eastern Bhutan where such klippen (Dang Chu-Zhemgang and Ura klippe) are thinner.

Further to the south, the high-velocity anomaly (hiW) in western Bhutan continues beneath the Paro window as a subhorizontal high shear-wave velocity zone (~3.6 km/s) between 10 and 15 km depth (Figure 8a). This high-velocity zone in the core of the Paro window above the MHT (Figure 8c) could reflect

subgreenschist facies LHS rocks piled into hinterland dipping duplexes [*Tobgay et al*., 2012] or an antiformal stack like in the Rangit window in Sikkim [*Bhattacharyya and Mitra*, 2009], which presumably led to the doming of the GHS and formation of the Paro window. Toward the north, the hiW anomaly reaches as shallow as 6 km depth directly above the southern edge of the MHT ramp. This ramp structure was imaged by previous studies, by receiver functions [*Singer et al*., 2017], by the Tib-1 reflection profile of the INDEPTH experiment [*Hauck et al*., 1998] northwest of Bhutan and defined by thermokinematic models [*Coutand et al*., 2014]. The velocity anomaly (hiW) extends toward the north in depth along the ramp of the MHT (Figure 7a) and can be associated with thrust duplexing in relation to the midcrustal ramp of the MHT [e.g., *Avouac*, 2003; *Bollinger et al*., 2006; *Herman et al*., 2010]. Similar to the high-velocity anomaly in the north (hiN), this anomaly atop of the midcrustal ramp appears to exhibits a low vp/vs-ratio ∼1.65 (Figure 8a) and could represent quartzite-dominated rocks, which were accreted to the Himalayan wedge from the underthrusting Indian plate by forming thrust duplexes.

In eastern Bhutan, the high-velocity anomaly (hiE) beneath the western and northern part of the Kuru Chu half-window between 4 and 11 km depth, and located above the subhorizontal segment of the MHT (Figures 6b and 6e) coincides, similar to the Paro window in western Bhutan, with an underlying LHS duplex of subgreenschist facies rocks of the LHS [*Long et al*., 2012]. The duplexing of the LHS is associated with a north to northeast-trending and northeast-plunging antiform of the LHS units in the core of the Kuru Chu half-window, which, in combination with river incision, causes the distinct northward reentrant of the MCT by ∼45 km [*Gansser*, 1983; *Long et al*., 2011a]. Therefore, we propose that this isotropic upper crustal shear-wave velocity anomaly most likely reflects the quartzite dominated lithology of the Baxa and Diuri groups forming a tectonic duplex structure. The estimated low vp/vs-ratio of $<$1.71 in this area of almost 30 km south-north extent (Figure 7b) supports an accumulation of quartzite dominated lithology at the base of the orogenic wedge.

Both shear-wave velocity anomalies, hiE and hiW, are trending to the NNW (Figures 6b, 6d, and 8) consistent with the same trend of antiforms mapped at the surface [*Long et al*., 2011c]. In addition, the hiE velocity anomaly disappears within ∼30 km to the east (Figure 6), where at the surface the half-window is replaced by the Sakteng klippe of the TSS (labeled as 6 in Figure 1) suggesting a structural depression and eastward termination of the Kuru Chu duplexes.

This short along-strike extent of the duplexes in association with the Kuru Chu half-window and the Paro window and with distinct high-velocity anomalies, agrees with the absence of such high-velocity anomaly in central Bhutan. There, the surface geology is dominated by synformal klippen (i.e., structural basins) of low greenschist facies metasedimentary rocks of the TSS overlying the GHS, which may be caused by the absence of duplexes in this segment of the LHS (Figures 8b and 8c). This first-order along-strike variation in the upper crustal structure of the Bhutan Himalaya supports a regional-scale, west-east structural variation in the LHS proposed by *Long et al*. [2011b, 2012].

In general, clusters of seismicity recorded during the two years of the GANSSER network operation [*Diehl et al*., 2015, 2016] do not correlate with the high shear-wave velocity areas in eastern or western Bhutan (Figures 7a and 7b), which we interpret as specific tectonic structures of the Bhutan orogenic wedge. This might be only apparent and we do not exclude a seismogenic behavior of these tectonic structures associated with the velocity anomalies over a longer time period. The main microseismicity cluster in eastern Bhutan is located in a low shear-wave velocity zone (∼3.2 km/s) at around 12 km depth beneath the eastern part of the Kuru Chu half-window (profile EAST 2 in Figure 7) and east of the high-velocity anomaly and may be associated with the MHT. This segment of the MHT, which appears to be seismically active after the M_W6.1 earthquake of September 2009 could indicate either a 4–5 years long lasting aftershock sequence or a partially creeping segment of the MHT in this area. Low shear-wave velocities above and along this segment and the indication of a high vp/vs-ratio of around 1.80 in the surrounding of this subhorizontal band of seismicity (Figure 7c) could be interpreted as indications of a fault damage zone. However, in consideration of the current understanding of the interseismic coupling along MHT in this region [e.g., *Marechal et al*., 2016], additional seismological characteristics of this shear zone are needed to explicitly associate these velocity anomalies with the MHT.

4. Conclusion

We imaged the 3-D shear-wave velocity structure of the Himalayan orogenic wedge in Bhutan using ambient seismic noise. Group velocity measurements of Rayleigh waves in the period range 2–20 s are extracted

from two years noise cross correlations and inverted directly to a 3-D velocity model using a frequency-dependent ray tracing approach. The tomographic images reveal a clear sensitivity of surface waves to first-order upper crustal tectonic structures. We resolve velocity anomalies with a lateral extent of around 20–30 km and minimum thickness of 4 km between 4 and 18 km depth. The quality of the 3-D velocity model is assessed with synthetic tests, which confirm poorer resolution ability in east-west direction along the strike of the Bhutan Himalaya due to the heterogeneous station distribution.

Our ambient noise tomography results agree with the upper crustal minimum 1-D *S* wave velocity model derived from body waves. High shear-wave velocity anomalies of $\geq$ 3.6 km/s are defined within western Bhutan on top of the midcrustal ramp of the MHT and beneath the Paro window, in the northwestern part of the Kuru Chu half-window and in the area of the Kakhtang thrust in central and eastern Bhutan. These local velocity anomalies are likely related to quartzite-dominated rocks of the LHS or felsic migmatites of the GHS with intrusions of leucogranites as suggested by the surface geology.

The high-velocity anomaly above the MHT in eastern Bhutan correlates with the north to northeast-trending and northeast-plunging antiform of the LHS within the Kuru Chu half-window and might represent the proposed underlying duplex of the Baxa and Diuri group [*Long et al*., 2012] with quartzite-dominated lithology similar to a high-velocity anomaly beneath the Paro window. The high-velocity anomaly on top of the midcrustal ramp of the MHT further to the north in western Bhutan may indicate the local formation of thrust duplexes of quartzite-dominated rocks accreted to the Himalayan wedge from the underthrusting Indian plate.

In correlation with the pattern of alternating tectonic windows and klippen exposed in the Bhutan Himalaya (i.e., a structurally dome-and-basin geometry as indicated in Figure 8c), our results reflect an along-strike variations in the upper crustal collision structure and provide evidence for the formation and depth extent of localized duplexes at the base of the Himalayan orogenic wedge.

Acknowledgments

We thank our colleagues at the Department of Geology and Mines of the Kingdom of Bhutan for the support during the entire fieldwork and the GANSSER fieldwork team. We thank A. Mordret for the possibility to use his ANWSTOMO code to compute 2-D surface wave group velocity maps. We thank L. Ermert for her help and comments on the seismic ambient noise pre-processing procedure. Discussions with T. Diehl on the seismic velocity structure are greatly appreciated. D. Grujic acknowledges the financial support of the ETH Zurich visiting professorship fond during his sabbatical stay at the ETH Zurich. H. Fang acknowledges the financial support from the Chinese Scholarship Council (CSC) for studying abroad at the ETH Zurich. We thank the two anonymous reviewers for their helpful comments on the manuscript. This work and the deployment of the temporary seismic GANSSER network in Bhutan was funded by the Swiss National Science Foundation (SNF), Grant 200021_143467 of G. Hetényi. The new seismic dataset recorded by the GANSSER network in 2013 and 2014 will be accessible online (http://stations.seddbd.ethz.ch/networks/xa/ or https://doi.org/10.12686/sed/networks/xa) by the end of 2017.

References

An, M., M. Feng, and Y. Zhao (2009), Destruction of lithosphere within the north China craton inferred from surface wave tomography, *Geochem. Geophys. Geosyst.*, *10*, Q08016, doi:10.1029/2009GC002562.

Avouac, J.-P. (2003), Mountain building, erosion, and the seismic cycle in the Nepal Himalaya, in *Advances in Geophysics*, vol. 46, edited by R. Dmowska, pp. 1–80, Elsevier, San Diego, Calif., doi:10.1016/S0065-2687(03)46001-9.

Barmin, M. P., M. H. Ritzwoller, and A. L. Levshin (2001), *A Fast and Reliable Method for Surface Wave Tomography*, pp. 1351–1375, Birkhauser, Basel.

Bensen, G. D., M. H. Ritzwoller, M. P. Barmin, A. L. Levshin, F. Lin, M. P. Moschetti, N. M. Shapiro, and Y. Yang (2007), Processing seismic ambient noise data to obtain reliable broad-band surface wave dispersion measurements, *Geophys. J. Int.*, *169*(3), 1239–1260, doi:10.1111/j.1365-246X.2007.03374.x.

Berthet, T., G. Hetényi, R. Cattin, S. N. Sapkota, C. Champollion, T. Kandel, E. Doerflinger, D. Drukpa, S. Lechmann, and M. Bonnin (2013), Lateral uniformity of India Plate strength over central and eastern Nepal, *Geophys. J. Int.*, *195*(3), 1481–1493, doi:10.1093/gji/ggt357.

Bhattacharyya, K., and G. Mitra (2009), A new kinematic evolutionary model for the growth of a duplex—An example from the Rangit duplex, Sikkim Himalaya, India, *Gondwana Res.*, *16*(3–4), 697–715, doi:10.1016/j.gr.2009.07.006.

Bollinger, L., P. Henry, and J. Avouac (2006), Mountain building in the Nepal Himalaya: Thermal and kinematic model, *Earth Planet. Sci. Lett.*, *244*(1–2), 58–71, doi:10.1016/j.epsl.2006.01.045.

Bookhagen, B., and D. W. Burbank (2010), Toward a complete Himalayan hydrological budget: Spatiotemporal distribution of snowmelt and rainfall and their impact on river discharge, *J. Geophys. Res.*, *115*, F03019, doi:10.1029/2009JF001426.

Boschi, L., and G. Ekström (2002), New images of the Earth's upper mantle from measurements of surface wave phase velocity anomalies, *J. Geophys. Res.*, *107*(B4), 2059, doi:10.1029/2000JB000059.

Brocher, T. M. (2005), Empirical relations between elastic wavespeeds and density in the Earth's crust, *Bull. Seismol. Soc. Am.*, *95*(6), 2081–2092, doi:10.1785/0120050077.

Burbank, D. W., R. A. Beck, and T. Mulder (1996), *The tectonic evolution of Asia*, in *The Himalayan Foreland Basin*, chap. 9, edited by A. Yin and T. M. Harrison, Cambridge Univ. Press Cambridge, U. K.

Caldwell, W. B., S. L. Klemperer, J. F. Lawrence, S. S. Rai, and Ashish (2013), Characterizing the Main Himalayan Thrust in the Garhwal Himalaya, India with receiver function CCP stacking, *Earth Planet. Sci. Lett.*, *367*, 15–27, doi:10.1016/j.epsl.2013.02.009.

Christensen, N. I. (1996), Poisson's ratio and crustal seismology, *J. Geophys. Res.*, *101*(B2), 3139–3156, doi:10.1029/95JB03446.

Coutand, I., D. M. Whipp, D. Grujic, M. Bernet, M. G. Fellin, B. Bookhagen, K. R. Landry, S. K. Ghalley, and C. Duncan (2014), Geometry and kinematics of the Main Himalayan Thrust and Neogene crustal exhumation in the Bhutanese Himalaya derived from inversion of multithermochronologic data, *J. Geophys. Res. Solid Earth*, *19*(2), 1446–1481, doi:10.1002/2013JB010891.

Diehl, T., J. Singer, G. Hetényi, E. Kissling, and J. F. Clinton (2015), Along-strike differences of the main Himalayan thrust and deformation within the Indian Crust: Insights from Seismicity and Seismic Velocities in Bhutan and its Foreland, Abstract #T21C-2833 presented at 2015 Fall Meeting, AGU, San Francisco, Calif.

Diehl, T., J. Singer, G. Hetényi, D. Grujic, J. Clinton, and E. Kissling (2016), The seismic gap of Bhutan: Evidence for segmentation of the Himalayas and its link to foreland deformation, paper presented at Himalayan-Karakorum-Tibet Workshop, Aussois, France, 9–12 May.

Fang, H., H. Yao, H. Zhang, Y.-C. Huang, and R. D. van der Hilst (2015), Direct inversion of surface wave dispersion for three-dimensional shallow crustal structure based on ray tracing: Methodology and application, *Geophys. J. Int.*, *201*(3), 1251–1263, doi:10.1093/gji/ggv080.

Gansser, A. (1983), *Geology of the Bhutan Himalaya*, Birkhauser, Basel.

Gritto, R., S.-H. Yoo, and S. P. Jarpe (2013), Three-dimensional seismic tomography at the Geysers geothermal field, CA, USA, in Proceedings of the Thirty-Eighth Work- shop on Geothermal Reservoir Engineering, February 1113, SGP-TR-198, Stanford University, Stanford, CA, pp. 1–12.

Grujic, D., C. J. Warren, and J. L. Wooden (2011), Rapid synconvergent exhumation of Miocene-aged lower orogenic crust in the eastern Himalaya, *Lithosphere*, *3*(5), 346–366, doi:10.1130/L154.1.

Guo, Z., X. Gao, H. Yao, J. Li, and W. Wang (2009), Midcrustal low-velocity layer beneath the central Himalaya and southern Tibet revealed by ambient noise array tomography, *Geochem. Geophys. Geosyst.*, *10*, Q05007, doi:10.1029/2009GC002458.

Hammer, P., T. Berthet, G. Hetényi, R. Cattin, D. Drukpa, J. Chophel, S. Lechmann, N. L. Moigne, C. Champollion, and E. Doerflinger (2013), Flexure of the India plate underneath the Bhutan Himalaya, *Geophys. Res. Lett.*, *40*, 4225–4230, doi:10.1002/grl.50793.

Hauck, M. L., K. D. Nelson, L. D. Brown, W. Zhao, and A. R. Ross (1998), Crustal structure of the Himalayan orogen at ~90° east longitude from Project INDEPTH deep reflection profiles, *Tectonics*, *17*(4), 481–500, doi:10.1029/98TC01314.

Herman, F., et al. (2010), Exhumation, crustal deformation, and thermal structure of the Nepal Himalaya derived from the inversion of thermochronological and thermobarometric data and modeling of the topography, *J. Geophys. Res.*, *115*, B06407, doi:10.1029/2008JB006126.

Herrmann, R. B. (2013), Computer programs in seismology: An evolving tool for instruction and research, *Seismol. Res. Lett.*, *84*(6), 1081–1088, doi:10.1785/0220110096.

Hetényi, G., et al. (2016), Segmentation of the Himalayas as revealed by arc-parallel gravity anomalies, *Sci. Rep.*, *6*, 33866, doi:10.1038/srep33866.

Huang, G. D., F. T. Wu, S. W. Roecker, and A. F. Sheehan (2009), Lithospheric structure of the central Himalaya from 3-D tomographic imaging, *Tectonophysics*, *475*, 524–543, doi:10.1016/j.tecto.2009.06.023.

Husen, S., T. Diehl, and E. Kissling (2009), The effects of data quality in local earthquake tomography: Application to the Alpine region, *Geophysics*, *74*(6), WCB71–WCB79, doi:10.1190/1.3237117.

Kellett, D., D. Grujic, and S. Erdmann (2009), Miocene structural reorganization of the South Tibetan detachment, eastern Himalaya: Implications for continental collision, *Lithosphere*, *1*(5), 259–281.

Kellett, D., D. Grujic, C. Warren, and J. Cottle (2010), Metamorphic history of a syn convergent orogen-parallel detachment: The South Tibetan detachment system, Bhutan Himalaya, *J. Metamorph. Geol.*, *28*, 785–808, doi:10.1111/j.1525-1314.2010.00893.x.

Kellett, D. A., and D. Grujic (2012), New insight into the South Tibetan detachment system: Not a single progressive deformation, *Tectonics*, *31*, TC2007, doi:10.1029/2011TC002957.

Kissling, E. (1988), Geotomography with local earthquake data, *Rev. Geophys.*, *26*, 659–698, doi:10.1029/RG026i004p00659.

Kissling, E., S. Husen, and F. Haslinger (2001), Model parametrization in seismic tomography: A choice of consequence for the solution quality, *Phys. Earth Planet. Inter.*, *123*, 89–101, doi:10.1016/S0031-9201(00)00203-X.

Landry, K. R., I. Coutand, D. M. Whipp, D. Grujic, and J. K. Hourigan (2016), Late neogene tectonically driven crustal exhumation of the Sikkim Himalaya: Insights from inversion of multithermochronologic data, *Tectonics*, *35*, 833–859, doi:10.1002/2015TC004102.

Levshin, A., T. Yanovskaya, A. Lander, B. Bukchin, M. Barmin, L. Ratnikova, and E. Its (1989), Seismic surface waves in a laterally inhomogeneous Earth, *Mod. Approaches Geophys.*, *9*, 131–169.

Lin, F.-C., D. Li, R. W. Clayton, and D. Hollis (2013), High-resolution 3-D shallow crustal structure in Long Beach, California: Application of ambient noise tomography on a dense seismic array, *Geophysics*, *78*(4), Q45–Q56, doi:10.1190/geo2012-0453.1.

Long, S., N. McQuarrie, T. Tobgay, and D. Grujic (2011a), Geometry and crustal shortening of the Himalayan fold-thrust belt, eastern and central Bhutan, *Geol. Soc. Am. Bull.*, *123*(7–8), 1427–1447, doi:10.1130/B30203.1.

Long, S., N. McQuarrie, T. Tobgay, and J. Hawthorne (2011b), Quantifying internal strain and deformation temperature in the eastern Himalaya, Bhutan: Implications for the evolution of strain in thrust sheets, *J. Struct. Geol.*, *33*, 579–608, doi:10.1016/j.jsg.2010.12.011.

Long, S., N. McQuarrie, T. Tobgay, D. Grujic, and L. Hollister (2011c), Geologic map of Bhutan, *J. Maps*, *7*, 184–192, doi:10.4113/jom.2011.1159.

Long, S. P., N. McQuarrie, T. Tobgay, I. Coutand, F. J. Cooper, P. W. Reiners, J. Wartho, and K. V. Hodges (2012), Variable shortening rates in the eastern Himalayan thrust belt, Bhutan: Insights from multiple thermochronologic and geochronologic data sets tied to kinematic reconstructions, *Tectonics*, *31*, TC5004, doi:10.1029/2012TC003155.

Marechal, A., et al. (2016), Evidence of interseismic coupling variations along the Bhutan Himalayan arc from new GPS data, *Geophys. Res. Lett.*, *43*, 12,399–12,406, doi:10.1002/2016GL071163.

Monsalve, G., A. Sheehan, C. Rowe, and S. Rajaure (2008), Seismic structure of the crust and the upper mantle beneath the Himalayas: Evidence for eclogitization of lower crustal rocks in the Indian plate, *J. Geophys. Res.*, *113*, B08315, doi:10.1029/2007JB005424.

Mordret, A., M. Landès, N. M. Shapiro, S. C. Singh, P. Roux, and O. I. Barkved (2013), Near-surface study at the Valhall oil field from ambient noise surface wave tomography, *Geophys. J. Int.*, *193*(3), 1627–1643, doi:10.1093/gji/ggt061.

Nabelek, J., G. Hetenyi, J. Vergne, S. Sapkota, B. Kafle, M. Jiang, H. Su, J. Chen, B. Huang, and t. H.-C. Team (2009), Underplating in the Himalaya-Tibet collision zone revealed by the Hi-CLIMB experiment, *Science*, *325*(5946), 1371–1374, doi:10.1126/science.1167719.

Rai, S. S., K. Priestley, V. K. Gaur, S. Mitra, M. P. Singh, and M. Searle (2006), Configuration of the Indian Moho beneath the NW Himalaya and Ladakh, *Geophys. Res. Lett.*, *33*, L15308, doi:10.1029/2006GL026076.

Rawlinson, N., and M. Sambridge (2004), Wave front evolution in strongly heterogeneous layered media using the fast marching method, *Geophys. J. Int.*, *156*, 631–647, doi:10.1111/j.1365-246X.2004.02153.x.

Roux-Mallouf, R., et al. (2015), Evidence for a wide and gently dipping Main Himalayan Thrust in western Bhutan, *Geophys. Res. Lett.*, *42*, 3257–3265, doi:10.1002/2015GL063767.

Sheehan, A. F., T. L. de la Torre, G. Monsalve, G. A. Abers, and B. R. Hacker (2014), Physical state of Himalayan crust and uppermost mantle: Constraints from seismic attenuation and velocity tomography, *J. Geophys. Res. Solid Earth*, *119*, 567–580, doi:10.1002/2013JB010601.

Sheen, D.-H., and J. S. Shin (2016), Observation of continuous microseismic P waves in Asia, *J. Geophys. Res. Solid Earth*, *121*, 248–259, doi:10.1002/2015JB012420.

Singer, J., E. Kissling, T. Diehl, and G. Hetényi (2017), The underthrusting Indian crust and its role in collision dynamics of the Eastern Himalaya in Bhutan: Insights from receiver function imaging, *J. Geophys. Res. Solid Earth*, *122*, doi:10.1002/2016JB013337.

Stöcklin, J. (1980), Geology of Nepal and its regional frame: Thirty-third William Smith Lecture, *J. Geol. Soc.*, *137*(1), 1–34, doi:10.1144/gsjgs.137.1.0001.

Tobgay, T., N. McQuarrie, S. Long, M. J. Kohn, and S. L. Corrie (2012), The age and rate of displacement along the Main Central Thrust in the western Bhutan Himalaya, *Earth Planet. Sci. Lett.*, *319–320*, 146–158, doi:10.1016/j.epsl.2011.12.005.

Warren, C. J., D. Grujic, D. A. Kellett, J. Cottle, R. A. Jamieson, and K. S. Ghalley (2011), Probing the depths of the India-Asia collision: U-/Th-Pb monazite chronology of granulites from NW Bhutan, *Tectonics*, *30*, TC2004, doi:10.1029/2010TC002738.

Yang, Y., M. H. Ritzwoller, A. L. Levshin, and N. M. Shapiro (2007), Ambient noise Rayleigh wave tomography across Europe, *Geophys. J. Int.*, *168*(1), 259–274, doi:10.1111/j.1365-246x.2006.03203.x.

Young, M. K., N. Rawlinson, P. Arroucau, A. M. Reading, and H. Tkalčić (2011), High-frequency ambient noise tomography of southeast Australia: New constraints on Tasmania's tectonic past, *Geophys. Res. Lett.*, *38*, L13313, doi:10.1029/2011GL047971.

Zhang, J., P. Gerstoft, and P. D. Bromirski (2010), Pelagic and coastal sources of P-wave microseisms: Generation under tropical cyclones, *Geophys. Res. Lett.*, *37*, L15301, doi:10.1029/2010GL044288.